

The Climatic Effects of Large Injections of Atmospheric Smoke and Dust: A Study of Climate Feedback Mechanisms With One- and Three-Dimensional Climate Models

R. D. CESS

Laboratory for Planetary Atmospheres Research, State University of New York, Stony Brook

G. L. POTTER AND S. J. GHAN

Lawrence Livermore National Laboratory, University of California, Livermore

W. L. GATES

Department of Atmospheric Sciences, Oregon State University, Corvallis

We have employed two climate models for the purpose of qualitatively understanding climate forcing mechanisms and feedback processes associated with the injection of atmospheric smoke and dust (i.e., atmospheric perturbations due to a nuclear exchange). One of these models is the Oregon State University general circulation model (GCM), modified through the addition of a delta-Eddington solar radiation routine to accommodate the inclusion of smoke and dust. The second model is a radiative convective model (RCM), which mimics as closely as possible many of the processes portrayed by the GCM. The primary role of the RCM was that of an educational tool used to reveal climate forcing and response processes, which would explain the behavior of the more complex GCM. The RCM served this purpose extremely well. Specific features revealed by the RCM are summarized as follows. (1) Even for very modest smoke loading, convective coupling of the model's surface and troposphere was insufficient to produce conventional surface-troposphere climate forcing. However, this was not the case when the model's climate was changed by increasing the atmospheric carbon dioxide, by increasing the solar constant, or by the inclusion of natural tropospheric aerosols. (2) Because of the above, for smoke injection the model's climate responded to two distinctly different and opposing radiative forcing mechanisms: direct surface-troposphere heating and direct surface cooling. (3) For a progressive increase in smoke loading a transition occurred from dominant (but not governing) surface-troposphere forcing to dominant surface forcing, with this transition being the result of changes both in vertical convection and in infrared radiation incident upon the surface. (4) The above two processes further impacted the nature of the model's climate response to the dual forcing mechanisms, and interactively they produced quite unusual time-dependent behavior. For example, there were situations in which the short-term climate response to a smoke injection was that of surface cooling, whereas the long-term response was one of warming. This understanding of the RCM behavior greatly aided the interpretation of the GCM results under conditions where the smoke loading, the smoke vertical distribution, and the smoke single scattering albedo were both independently and simultaneously varied. The GCM's surface cooling further exhibited a marked dependence upon which day of the control run (a perpetual July) the smoke is injected.

1. INTRODUCTION

Recently, it has been suggested [Crutzen and Birks, 1982; Turco *et al.*, 1983] that substantial quantities of both smoke and dust might be injected into the atmosphere following a nuclear exchange; the smoke being produced by fires resulting from the exchange, while ground bursts in the vicinity of missile silos could inject significant quantities of dust directly into the stratosphere. Moreover, a number of studies have also appeared pertaining to the potential climatic impact of such atmospheric smoke/dust injections, and these have spanned the hierarchy of climate models, including one-dimensional models [Turco *et al.*, 1983; MacCracken, 1983; Crutzen *et al.*, 1984; Ramaswamy and Kiehl, 1985], a two-dimensional energy balance model [Robock, 1984], a two-dimensional statistical-dynamical model [MacCracken, 1983], and three-dimensional general circulation models [Aleksandrov and Stenchikov, 1983; Covey *et al.*, 1984, 1985; Thompson *et al.*, 1984; MacCracken and Walton, 1984].

For the most part these studies have focused upon the climatic impact due to specific scenarios involving atmospheric smoke/dust loadings. One exception is the work by Ramaswamy and Kiehl [1985], who performed sensitivity studies of radiative forcing by atmospheric smoke and dust. In addition, Covey *et al.* [1985] have investigated changes in model-simulated physical processes, using a general circulation model, as induced by a single smoke loading. But little attention has been directed yet toward how climate feedback processes operate when the climate forcing is as extreme and unusual as in the nuclear exchange scenarios.

As a prelude to understanding the type of climate forcing involved here it is instructive to subdivide climate change into a two-stage process. The first stage is the direct (or initial) radiative forcing that induces the change, such as infrared radiative forcing resulting from an increase in atmospheric CO₂ or solar radiative forcing resulting from a change of the solar constant, to cite two familiar examples. The second stage is the climate response to that forcing.

Prior to the nuclear exchange studies, it was conventional to interpret the climate forcing as the net radiative forcing of the surface-troposphere system [e.g., Dickinson, 1982; Potter and Cess, 1984]. This was because (at least within the model

Copyright 1985 by the American Geophysical Union.

Paper number 5D0708.
0148-0227/85/005D-0708\$05.00

studies used to arrive at this conclusion) the convective mixing within the troposphere essentially couples the surface and troposphere so that they act as a single thermodynamic system. Thus if the direct radiative forcing produces heating of the coupled surface-troposphere system, the resulting climate response would be that of surface warming.

But quite a different conclusion applies to the nuclear exchange studies [see Cess, 1985, for a more detailed discussion]. To illustrate this, we consider, for simplicity, the case of only smoke injection into the atmosphere. In all of the nuclear exchange studies the radiative properties of smoke were such that its presence within the atmosphere increased the absorption of solar radiation by the surface-troposphere system, and if our prior discussion was still applicable, then the smoke should have produced surface warming. But for the large smoke injections considered [Covey *et al.*, 1984, 1985; Ramaswamy and Kiehl, 1985], the models yielded significant surface cooling instead.

The reason for this rather contrary behavior of the models is that solar absorption by smoke produced strong warming of the atmosphere with a corresponding substantial reduction in solar radiation reaching the surface. This, in turn, increased the static stability of what had been the convective troposphere to such an extent that convective mixing was substantially reduced within that region, so that the surface and lower atmosphere (the lower atmosphere being the region that had originally been the convective troposphere) no longer behaved as a single thermodynamic system. Since convective processes cool the surface, this reduction of convective mixing would, by itself, lead to surface warming. But the reduction of solar radiation reaching the surface, as a consequence of smoke absorption, more than compensated for this. In addition the near elimination of convective mixing means that the surface temperature is now essentially governed by radiative processes. Thus the surface cooling is a consequence of the reduction in net radiation absorbed by the surface, with the direct radiative forcing arising from the reduction in solar radiation reaching the surface.

In summary, then, for large smoke loading the direct radiative forcing by smoke cools the surface and warms the troposphere, with the corresponding reduction in convective coupling of the surface and lower atmosphere rendering the direct surface forcing the relevant climate forcing mechanism, rather than surface-troposphere forcing. But one would anticipate that for small or modest smoke loading the surface-troposphere forcing should still dominate, since for small smoke loading there must still be significant convective coupling between the surface and the lower atmosphere. This suggests that as smoke loading is increased, a transition takes place from direct surface-troposphere forcing to direct surface forcing, with a corresponding transition from surface warming to surface cooling. A further interesting aspect of this effect concerns the role of climate feedback mechanisms. Conventionally, we think of such mechanisms as processes that modify the climatic response to a forcing. But in the present context they should additionally influence the transition from surface-troposphere forcing to surface forcing.

The purpose of the present investigation is twofold. The first goal is to employ the Oregon State University general circulation model (OSU GCM), together with an analog radiative convective model (RCM), as vehicles to study the interactive climate processes associated with the incorporation of atmospheric smoke as discussed above. In addition to serving as an aid in interpreting the OSU GCM results, the analog RCM

further allows an intercomparison between a GCM and a comparable RCM.

The second purpose of this study is to illustrate the sensitivity of the GCM's simulated climate change to changes in smoke loading, smoke vertical distribution, and smoke optical properties, all of which are highly uncertain with respect to the nuclear exchange scenarios, as well as incorporating the effects of atmospheric dust. It is emphasized that this second goal is by no means independent of the first, since the interpretation of the sensitivity studies requires knowledge as to how climate processes operate within the GCM.

2. MODEL DESCRIPTIONS

General Circulation Model

The OSU atmospheric general circulation model is unique among current GCM's in that it has only two interior tropospheric levels and no stratospheric simulation. This GCM therefore has the minimum vertical resolution necessary to depict the barocline structure of the atmosphere, but its physical and numerical sophistication is comparable to that of other models. Perhaps more importantly for the present application, its portrayal of the surface climate is fully competitive with that of models of higher resolution, and its integration speed permits the construction of experimental simulations with relative economy.

Although a complete documentation of the model has been given by Ghan *et al.* [1982], it is useful to briefly summarize its basic structure here. The model is formulated in the vertical σ coordinate system given by $\sigma = (p - p_t)/\pi$, where p is pressure, p_t is the constant pressure at the top of the model atmosphere (200 mbar), and $\pi = p_s - p_t$ is a measure of the variable surface pressure p_s . In this system the earth's surface ($p = p_s$) is everywhere given by $\sigma = 1$, and the top of the model ($p = p_t = 200$ mbar) is given by $\sigma = 0$. The tropospheric prognostic variables of the model are the horizontal velocity, the temperature, and the water vapor mixing ratio; each of these is carried at the two, equally spaced interior tropospheric levels $\sigma = 1/4$ and $\sigma = 3/4$. The surface pressure p_s is also a prognostic variable, as is the surface temperature, the ground wetness, and snow amount. In addition to these variables, certain additional quantities are determined diagnostically, such as the specific volume, the geopotential, and the vertical motion (σ). The basic equations governing these variables are the primitive (hydrostatic) equations of motion, the equations of continuity for mass and moisture, the thermodynamic energy equation, and the equation of state.

The boundary conditions accompanying this system apply at the top of the (model) atmosphere—where the incoming solar radiation is prescribed according to the latitude, time of day, and season, and the vertical motion is set to zero—and at the earth's surface, where the elevation, albedo, and sea-surface temperature (and sea ice) are prescribed. The model's equations are developed in terms of averages over the upper and lower halves of the model atmosphere and identified with the levels $\sigma = 1/4$ and $3/4$, and the local solutions are determined on a spherical grid of 4° latitude and 5° longitude resolution by a finite-difference procedure designed to conserve total energy and momentum (in the absence of sources and sinks). Details of these and related numerical aspects of the model are given in Ghan *et al.* [1982].

Since the model's performance is significantly influenced by the treatment of the friction, heating, and moisture, it is useful to briefly summarize these parameterizations along with the

parameterization of the cloudiness and the various surface processes. The frictional force consists of an internal transfer of momentum between the model's two levels (proportional to the vertical wind shear and the viscosity resulting from convection and background turbulence) and a surface stress which acts on the wind at the lower model level; the model has no explicit subgrid-scale lateral diffusion. The diabatic heating rate at the upper level contains the absorption of solar radiation in the upper layer (dependent upon the predicted clouds and water vapor mixing ratio), the net long-wave radiation lost from the layer (dependent on the predicted temperature, clouds, and mixing ratio), and the warming of the layer by the latent heat released. The heating rate at the lower level contains the corresponding quantities for the lower layer and, in addition, includes the surface sensible heat flux (dependent upon the ground-to-surface air temperature difference and the surface wind). The total condensation rate C at both model levels is the sum of that from both large-scale and convective-scale processes, the latter of which results from the model's convective adjustments required to maintain a stable lapse rate. The total precipitation P at the surface is taken equal to the net difference between the condensation and the evaporation from falling precipitation in the atmospheric column.

The surface boundary layer in the model is parameterized as a constant flux layer of undefined thickness. The turbulent surface fluxes of sensible heat and water vapor (i.e., the surface evaporation) are parameterized according to the bulk aerodynamic method, with the effective vertical diffusion coefficient dependent upon low-level stability. Cloudiness in the model is parameterized as a result of both large-scale and convective motions. Large-scale cloudiness occurs when the relative humidity exceeds 90% (100% for the upper layer), while the cloudiness resulting from convective motion is always overcast; the total cloudiness refers to all coexisting cloud types. Each type of simulated cloud has an assigned thickness and representative optical properties (see the appendix) and interacts with the transfer of both solar and long-wave radiation; cloud liquid water content and advection, however, are neglected (see the appendix for a summary of the cloudiness parameterization employed in the specific model version used here).

To accommodate the inclusion of atmospheric smoke and dust into the GCM, the solar radiation routine was replaced by a delta-Eddington model as described in the appendix. We neglect the infrared opacity of both smoke and dust, since *Ramaswamy and Kiehl* [1985] indicate that this is a second-order effect.

Radiative Convective Model

The RCM is designed to serve as a one-dimensional analog of the three-dimensional general circulation model; it can, in several respects, be considered a horizontally averaged version of the GCM. It uses the same vertical resolution, with prognostic variables carried only at $\sigma = 1/4$ and $3/4$. The treatment of infrared and solar radiation is identical in both models. The RCM also calculates the surface fluxes of sensible and latent heat in much the same manner as the GCM. Of special relevance to the present problem is the same dependence of the vertical eddy diffusivity on the stability of the surface layer in both models.

The models differ significantly in other respects, however. Whereas the GCM resolves latent heating and vertical sensible heat flux on the large (500-km) scale and uses an Arakawa parameterization for moist convection, the RCM lumps these

TABLE 1. Latitudinal Variation of Smoke Optical Depth

Latitude Range	Optical Depth Factor
0°–4°N	0
4°–8°N	0.2
8°–12°N	0.4
12°–16°N	0.6
16°–20°N	0.8
20°–90°N	1.0

The optical depth factor is the quantity by which the constant 20°–90°N optical depth is multiplied.

terms into a simple 6.5 K/km lapse rate adjustment. The hydrological cycle in the RCM is approximated by assuming a fixed relative humidity, neglecting all clouds, and prescribing the ground wetness to be 0.1. The vertical distribution of relative humidity is taken from *Manabe and Wetherald* [1967], with a surface relative humidity of 77%. The surface drag coefficient, which depends on the surface wind speed in the GCM, is prescribed in the RCM such that the surface exchange coefficient for sensible heat is $8 \text{ W C}^{-1} \text{ m}^{-2}$. The surface albedo is set equal to 0.2. Perhaps of greatest importance for the transient problem is the zero surface heat capacity in the RCM. In the GCM the surface heat capacity is infinite for the ocean and elsewhere is given a value appropriate for the diurnal cycle. Also, within the RCM the GCM's diurnal cycle was replaced by a 60° mean solar zenith angle.

3. MODEL SIMULATIONS

For the purpose of studying and understanding climate processes associated with the injection of atmospheric smoke it will be assumed within both the GCM and the RCM that the smoke single scattering albedo is 0.7 at a wavelength of 0.55 μm , while the smoke vertical distribution corresponds to a uniform atmospheric mixing ratio. Further details as to the smoke optical properties are given in the appendix.

With respect to sensitivity studies, which will be discussed in section 6, a 0.55 μm single scattering albedo of 0.5 will also be considered, as will a vertical distribution corresponding to a constant smoke density. The 0.5 and 0.7 values for the smoke single scattering albedo essentially span the range of values utilized in current nuclear exchange scenarios.

The horizontal smoke distribution employed within the GCM is assumed to be a uniform distribution over longitude, while the latitudinal distribution of smoke optical depth is listed in Table 1, where the normalized optical depth is referenced to a constant optical depth for the latitude range 20°–90°N.

With one exception the GCM simulations are performed with average July insolation at the top of the model and with fixed sea surface temperatures. *Covey et al.* [1985] found the maximum climatic impact for a summer simulation, and this was our motivation for choosing July. The exception is that, for the purpose of intercomparing the GCM and RCM, April GCM simulations will also be performed since, as discussed in section 5, this allows a more appropriate model intercomparison. In that we are investigating only short-term climatic effects, it suffices to employ fixed sea-surface temperatures.

The control run consists of a 100-day perpetual July (or April) simulation, while the perturbed simulations utilize initial conditions from day 90 of the control, at which time smoke is introduced into the model, and the smoke loading is kept constant with time during an ensuing 10-day model run.

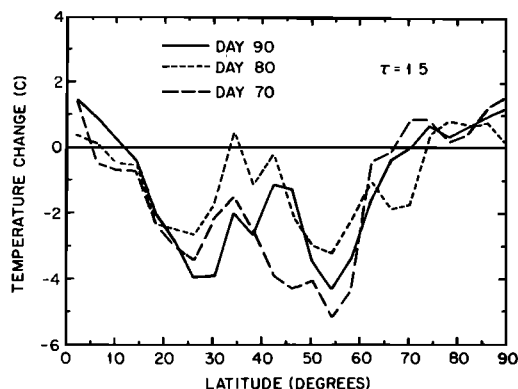


Fig. 1. Zonally averaged (over land and sea-ice areas) changes in July surface-air temperature for a smoke optical depth of 1.5 and for three different times at which smoke is injected into the control climate. These results refer to day 10 following the smoke injection.

We will mainly focus upon the climatic change occurring on day 10 of the perturbed run, with this change being determined by referencing to day 100 of the control run. In this way we are comparing two simulations (control and perturbed) that have the same initial conditions (day 90 of the control) and the same duration (10 days).

Since a GCM, like the real climate system, has considerable synoptic variability, our simulated climate change will be dependent upon the arbitrarily chosen initial conditions (day 90 of the control). To illustrate this, we have performed a limited number of simulations in which the perturbed runs employed initial conditions from days 70 and 80 of the control, with day 10 of these perturbed runs being referenced to days 80 and 90, respectively, of the control. The changes in the model's surface-air temperature, zonally averaged over land areas (and over sea ice), are shown in Figure 1 as a function of latitude for a 20°–90°N smoke optical depth τ of 1.5. (Here, and throughout the rest of this paper, the optical depth refers to the constant 20°–90°N value, with the latitudinal variability being that given in Table 1.) Note the presence of synoptic variability in these three simulations because of the different initial conditions; such variability is representative of that to be expected by natural fluctuations in the climate system as presented by a GCM.

But this dependence upon initial conditions is considerably

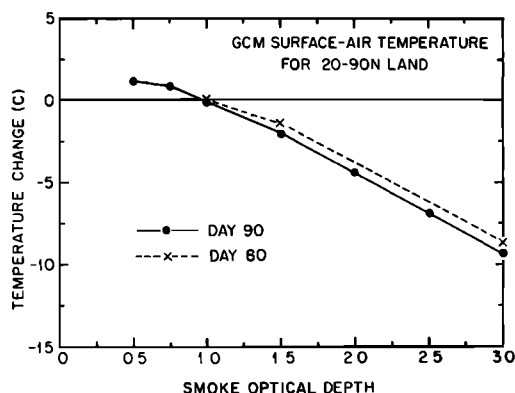


Fig. 2. Changes in day 10 surface-air temperature as a function of smoke optical depth for land and sea-ice areas averaged from 20°N to 90°N and for smoke injection on days 80 and 90 of the July control climate.

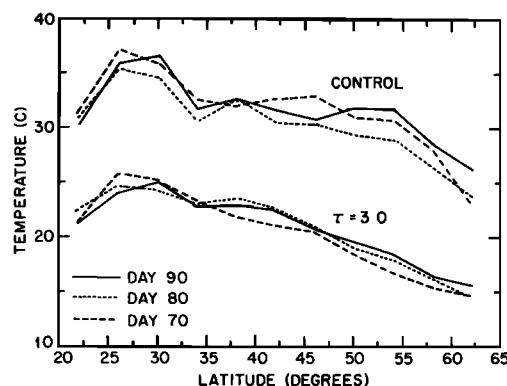


Fig. 3. July surface-air temperature, zonally averaged over land and sea-ice areas, for both the control climate and a smoke optical depth of 3 and for three different times of smoke injection. All results refer to day 10 following the smoke injection. Thus the control curve for day 90 actually refers to day 100 of the control run.

reduced when latitudinal averaging is performed. Figure 2 illustrates 20°–90°N land (and sea-ice) averages, as a function of smoke optical depth, which correspond to the latitude range over which the smoke optical depth is uniform. We have also obtained results by using initial conditions from day 70 of the control, but these are not shown in Figure 2, since they are virtually identical to the day 90 results.

The main point of Figures 1 and 2 is that it is not meaningful to intercompare general circulation models on a latitudinal basis, unless either statistical ensembles or several-day averages are used, because of the strong initial condition and latitude dependence of the changes in zonally averaged surface-air temperature. This problem is greatly minimized, however, when latitudinal averaging is performed.

A further point is that synoptic variability over the land areas diminishes as smoke loading increases because of increasingly stable stratification. This is illustrated in Figure 3 with respect to the latitudinal variability of land-averaged surface-air temperature for the three control runs and for the corresponding $\tau = 3$ runs.

With regard to the one-dimensional RCM, the simulations were performed for both equilibrium conditions (i.e., an equilibrium perturbed climate will be compared to an equilibrium control climate) and for day 10. In that this model has only a single horizontal grid point, the smoke optical depth refers here to a globally averaged quantity.

4. RADIATIVE CONVECTIVE MODEL RESULTS

As discussed in the introduction, it has been conventional to interpret climate forcing as the net radiative forcing of the surface-troposphere system; we therefore first employ the RCM to illustrate some rather interesting aspects of this interpretation. Letting F and Q denote the net upward infrared and net downward solar radiative fluxes, respectively, at the top of the model's atmosphere, then on the global annual average, which applies to the RCM simulations, the radiative energy balance is $F = Q$.

Consider now that the surface-troposphere system is perturbed by an energy flux G . It follows that the ensuing global climate response, defined here in terms of global surface temperature T_g , is

$$\Delta T_g = \lambda \times G \quad (1)$$

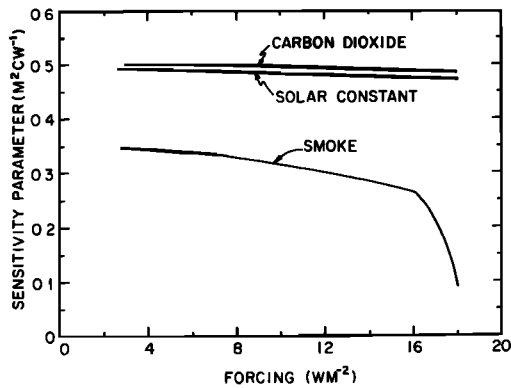


Fig. 4. Climate sensitivity parameters for the RCM as a function of the direct surface-troposphere radiative forcing, for climate change induced by an increase in the atmospheric carbon dioxide content, for an increase in the solar constant, and for the injection of atmospheric smoke.

where λ is a climate sensitivity parameter given by

$$\frac{1}{\lambda} = \frac{dF}{dT_g} - \frac{dQ}{dT_g} \quad (2)$$

and it is this quantity that incorporates climate feedback mechanisms [e.g., Cess, 1976]. If λ is essentially independent of both the type of forcing (e.g., a change in solar constant as opposed to a change in atmospheric carbon dioxide content) and the magnitude of the forcing, then the surface-troposphere system responds as a single thermodynamic system as a result of the convective coupling of the surface and troposphere. This, of course, is the assumption upon which (1) and (2) are based, since G denotes the forcing of the coupled system.

To illustrate whether or not λ , as evaluated from the RCM, is invariant upon the type of climate forcing, we consider three distinctly different type of forcings. These consist of an increase in the solar constant, an increase in atmospheric carbon dioxide content, and the addition of atmospheric smoke. The solar constant increase produces a positive solar radiation forcing of the surface-troposphere system, while the carbon dioxide increase results in a positive infrared forcing. As discussed in section 2, we have incorporated only solar radiation influences resulting from atmospheric smoke, and the sign of the forcing will be dependent upon the smoke's single scattering albedo [e.g., Coakley et al., 1983]. As will be shown below, the presently employed single scattering albedo of 0.7 produces surface-troposphere warming such that all three forcings have the same sign.

The surface-troposphere forcings have been evaluated for each of the climate change cases by running the RCM through a single time step in order to isolate the initial radiative impact of the respective forcing while holding all other climate parameters fixed at their control values. These forcings, together with the corresponding equilibrium ΔT_g values, were then used to evaluate λ from (1); the results are summarized in Figure 4.

Recall that if λ is essentially independent of both the type of forcing and the magnitude of the forcing, then the surface-troposphere system responds as a single coupled system. The solar constant and carbon dioxide results shown in Figure 4 are consistent with this interpretation. The modest dependence of these results upon forcing is actually due to climate feedback mechanisms being climate state dependent, as manifested within (2). Moreover, the slight difference between the

solar constant and carbon dioxide results for λ is attributable to second-order feedback processes. For example, warming attributable to an increase in solar constant results in a corresponding increase in atmospheric water vapor content, producing the well-known water vapor feedback inherent within (2). But a second-order feedback, not included within (2), is the modification of the initial solar constant forcing by the change in planetary albedo resulting from increased atmospheric water vapor.

Returning to the matter of surface-troposphere coupling, for increasing carbon dioxide, roughly 75% of the surface-troposphere heating is tropospheric heating, while for the solar constant increase it is about 25%. Thus, although the surface/troposphere partitioning of the forcings differs considerably, the nearly identical sensitivity parameters indicates that it is surface-troposphere forcing that governs the response of the RCM for these simulations.

Quite a different conclusion applies for the addition of atmospheric smoke. Here the sensitivity parameter is considerably different than in the two other cases, indicating that even for small smoke loading the surface and troposphere are not responding as a coupled system. This is because, as discussed in the introduction, the direct radiative forcing by smoke cools the surface but warms the troposphere, and the convective coupling of the model's surface and troposphere is not sufficient, even for small smoke loading, to overcome this.

To avoid possible future confusion, it must be emphasized that the smoke sensitivity results of Figure 4 are strongly dependent upon the type of radiative convective model employed. To give an example of this, we have also used a degraded version of the RCM that utilizes the more conventional, although less realistic, assumption that there is no distinction between surface-air and ground temperatures; i.e., the boundary layer parameterization has been removed. In this version of the RCM the smoke sensitivity parameter is virtually identical to the carbon dioxide and solar constant results (Figure 4) when the forcing is less than 10 W m^{-2} .

It should also be emphasized that the results of Figure 4 do not contradict Potter and Cess [1984], who employed a statistical-dynamical model to show that the inclusion of natural tropospheric aerosols was consistent with the assumption of surface-troposphere forcing. The difference between our and their conclusions is due to differences in aerosol optical properties, with our smoke model absorbing significantly more solar radiation than their model for tropospheric aerosols. To test this, a single scattering albedo of 0.95 (roughly appropriate for natural tropospheric aerosols) was also employed within the RCM, and this produced a sensitivity parameter similar to the carbon dioxide and solar constant results of Figure 4.

As was discussed in the introduction, one would anticipate that for increasing smoke loading a transition should occur from dominant surface-troposphere forcing to dominant surface forcing, and Figure 4 can best be explained within this framework. Since the smoke λ is positive for the forcing range shown in Figure 4, then surface warming will occur and surface-troposphere heating dominates as the forcing mechanism, but with direct surface cooling moderating this surface warming, since there is incomplete convective coupling of the surface and troposphere. Continuing beyond the forcing range shown in Figure 4, at a forcing of approximately 18 W m^{-2} the sensitivity parameter is zero, indicating that the two forcing mechanisms are compensating one another; beyond this a negative λ means that direct surface forcing dominates. The abrupt change at 16 W m^{-2} corresponds to a smoke optical

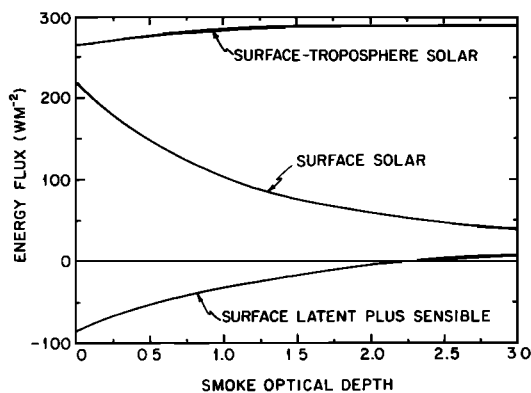


Fig. 5. The RCM's equilibrium surface-troposphere solar absorption, surface solar absorption, and latent plus sensible surface heat flux as a function of smoke optical depth.

depth of unity; this is due to an interesting climate feedback process which will shortly be discussed.

Figure 5 serves to further illustrate this rather unusual forcing transition. Shown here are the direct surface-troposphere and surface forcings associated with increasing smoke optical depth as well as the corresponding change in surface (latent plus sensible) fluxes. As optical depth increases, the transition from dominant surface-troposphere forcing (heating) to dominant surface forcing (cooling) occurs as a result of the associated reduction in convective coupling between the surface and troposphere, which is in turn a consequence of the two direct forcings producing an increase in atmospheric static stability. A comparable sequence of events does not occur for increasing atmospheric carbon dioxide. Instead, a carbon dioxide increase leads to enhanced convective coupling of the surface and troposphere.

Before proceeding, it is useful to clarify our terminology of surface-troposphere forcing. Here the use of "troposphere" refers to what had been the troposphere within the model's control climate. For large smoke optical depths a conventional convective troposphere no longer exists within the model.

A further point concerning the forcing transition is that the nature of the transition is highly dependent upon an associated feedback process. In Figure 6 we show the changes, as a function of optical depth, in surface solar absorption, surface infrared absorption, and net (solar plus infrared) surface absorption. As optical depth increases, the corresponding atmo-

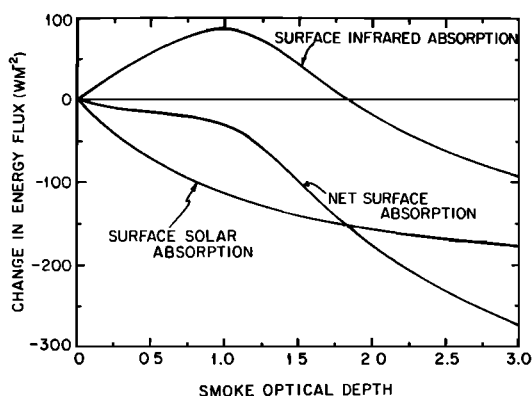


Fig. 6. Changes in the RCM's equilibrium surface solar absorption, surface infrared absorption, and net surface absorption as a function of smoke optical depth.

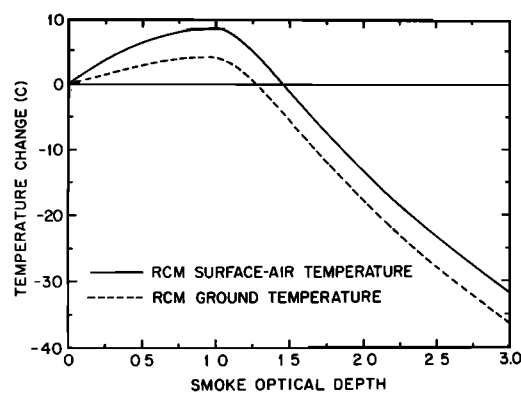


Fig. 7. Equilibrium changes in the RCM's surface-air temperature and ground temperature as a function of smoke optical depth.

spheric heating results in an increase in incident infrared radiation at the surface; this increase continues to an optical depth of unity and largely compensates for the reduction in surface solar absorption. Since the surface is responding to both the direct solar forcing and the associated infrared response, it is the net surface absorption that is of importance. This explains the forcing $<16 \text{ W m}^{-2}$ result in Figure 4. While the dominant surface-troposphere heating produces a positive sensitivity parameter, the secondary net surface absorption (forcing plus response) induces a gradual surface cooling with increasing optical depth, which is the explanation for the downward drift of the sensitivity parameter (Figure 4).

Beyond an optical depth of unity (forcing $>16 \text{ W m}^{-2}$), the surface infrared absorption begins to decrease because of atmospheric solar absorption by smoke occurring at progressively higher altitudes, where it is more efficiently reemitted to space and less efficiently reemitted downward to the surface. This causes the abrupt reduction in the net surface absorption (Figure 6) that is the explanation for the corresponding abrupt reduction of the sensitivity parameter (Figure 4). Recall that the variation of the sensitivity parameter with optical depth is related to the transition from dominant surface-troposphere forcing to dominant surface forcing. Thus an important conclusion of this analysis is that this transition process is tightly coupled to the associated infrared response.

Figure 7 illustrates the equilibrium response of both ground temperature and surface-air temperature for the RCM. Consistent with the prior discussion concerning forcing, there is surface warming for modest optical depths, while at large optical depths there is substantial surface cooling. Note the significantly different behavior of ground temperature versus surface-air temperature. This has also been observed by Covey *et al.* [1985] in their GCM study, and it is a consequence of the direct radiative forcing by smoke heating the atmosphere but cooling the surface. For both solar constant and carbon dioxide forcing, this difference is greatly diminished.

In Figure 8 the equilibrium surface-air temperature response of Figure 7 is compared with the day 10 response, while the time history for the first 30 days of the RCM's surface-air temperature change is illustrated in Figure 9 for $\tau = 1.0, 1.84$, and 3.0 . These results are quite surprising. In essence the transient response of the RCM, categorized for different ranges of smoke optical depth τ , may be summarized as follows.

1. For $\tau < 1.5$ the equilibrium response is that of warming (i.e., an increase in surface-air temperature), whereas it is cool-

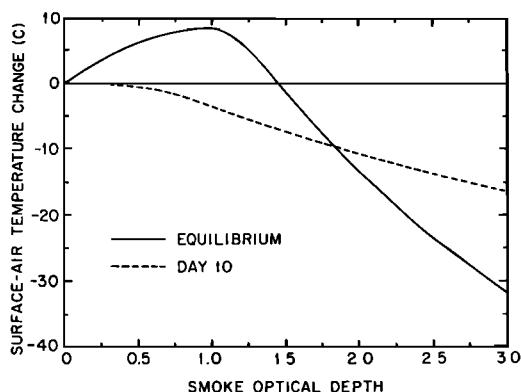


Fig. 8. Equilibrium and day 10 changes in the RCM's surface-air temperature as a function of smoke optical depth.

ing for the day 10 response. As is illustrated by the $\tau = 1$ curve of Figure 9, this coincides with an entire time history in which there is initial cooling followed by a reversal, with surface-air temperature subsequently passing through the control value and then asymptotically approaching the equilibrium warming.

2. For $1.5 < \tau < 1.8$ the small-time response overshoots the equilibrium cooling, then reverses and asymptotically approaches equilibrium cooling.

3. For $\tau > 1.8$ the time history is more conventional, with a monotonic approach to equilibrium cooling (Figure 9).

The unusual $\tau < 1.8$ behavior can be explained in terms of the time-dependent nature of the surface infrared absorption, which will be governed by atmospheric time constants, since this involves an absorption of downward emitted radiation from the atmosphere. Thus there will be no immediate response of this quantity at the time of smoke injection, but as time progresses, a time-dependent evolution to the equilibrium results shown in Figure 6 will occur. The surface solar absorption, on the other hand, will be nearly invariant with time, since only a second-order modification of this quantity takes place because of changes in atmospheric water vapor content.

With reference to Figure 6 this means that in proceeding from the initial smoke injection to the final equilibrium climate, the time-dependent net surface absorption essentially progresses from the surface solar absorption curve to the equilibrium net surface absorption curve. This explains the behavior for $\tau < 1.5$ discussed above. The initial reduction in net surface absorption produces sufficient convective decoupling of the surface and troposphere so that direct surface forcing is the dominant climate forcing mechanism, producing a decrease in surface-air temperature. As time progresses, the subsequent warming of the atmosphere causes an increase in surface infrared absorption, modifying the cooling and simultaneously producing a progressive enhancement of convective coupling so that there is a time-dependent transition from dominant surface forcing to dominant surface-troposphere forcing, with the latter causing an increase in surface-air temperature throughout the later stages of the transient process.

A comparable explanation applies for the $1.5 < \tau < 1.8$ overshoot cooling. Here, direct surface cooling dominates at all times, but by the mechanisms just discussed, following the initial perturbation (smoke injection), there is a time-dependent change in net surface absorption such that this quantity is greater at equilibrium than on day 10.

The $\tau = 1.8$ intersection (actually $\tau = 1.84$) of the day 10

and equilibrium curves (Figure 8) produces another unusual result. This intersection coincides with the intersection of the surface solar absorption and net surface absorption curves of Figure 6, which implies that there is essentially no time-dependent change in surface infrared absorption, because of simultaneous changes in the vertical distributions of both atmospheric temperature and water vapor. Thus for $\tau = 1.84$ the surface response is radiatively decoupled from atmospheric time constant. The 30-day time history for $\tau = 1.84$ (Figure 9) is consistent with this interpretation, and the surface climate reaches near equilibrium within just a few days.

The $\tau = 1$ and $\tau = 3$ curves of Figure 9, on the other hand, show the more conventional long (much greater than 30 days) approach to equilibrium [e.g., Manabe and Wetherald, 1967]. But nevertheless there is a very rapid initial response to smoke injection because of the initial reduction in surface absorbed solar radiation, and this will later be shown to be characteristic also of two different general circulation models.

In closing this section we reemphasize that we are employing the RCM solely for the purpose of gaining a qualitative insight into how climate processes operate under various smoke loadings. A notable finding is the important role played by the incident infrared flux at the surface. Not only does this impact the relative importance of surface-troposphere versus surface forcing, but it also affects, as a feedback process, the climate response to these forcings; in addition it strongly impacts the transient response of the model.

5. MODEL INTERCOMPARISONS

One purpose of the present paper is to intercompare the climatic response of the GCM and that of the analog RCM. But before doing this, we first take advantage of the fact that Covey *et al.* [1984, 1985] have performed a simulation of the climatic impact caused by a large injection of atmospheric smoke by employing the National Center for Atmospheric Research Community Climate Model (NCAR CCM), and this conveniently allows an intercomparison of two general circulation models, i.e., the NCAR CCM and the OSU GCM.

In their simulation, Covey *et al.* [1984, 1985] assumed the smoke to be purely absorbing, which corresponds to employing a smoke single scattering albedo of zero within the OSU GCM. Furthermore, they located the smoke, having an optical depth of 3, within the latitude range 31° – 67° N and uniformly distributed over longitude. Because of differences in the horizontal resolution of the two models, this translates, for

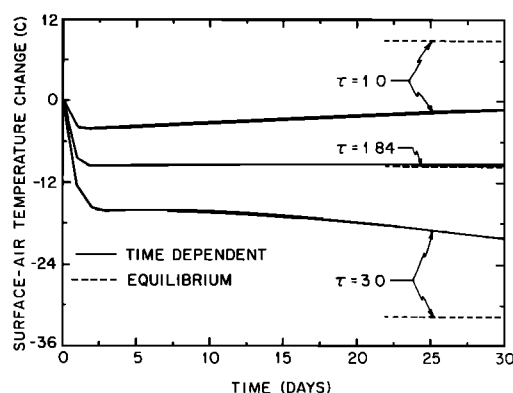


Fig. 9. Time evolutions of the RCM's changes in surface-air temperature for the smoke optical depths of $\tau = 1.0$, 1.84, and 3.0. The horizontal dashed lines denote the equilibrium temperature change. Smoke is injected on day 0.

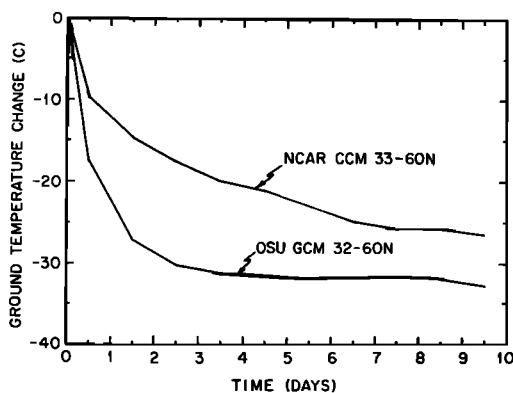


Fig. 10. Comparison of the time evolutions of the OSU GCM and NCAR CCM [Covey *et al.*, 1985] changes in July ground temperature averaged over the indicated latitudes. The CCM results refer to elapsed time, whereas for the OSU GCM, 24-hour averages are plotted at half days (e.g., the 24-hour average of day 1 is plotted at 0.5 days). For both models, smoke is injected at day 0.

the OSU GCM, to smoke located within the latitude range 32°–68°N. Moreover, Covey *et al.* incorporated a smoke optical depth of 1.5 at the edges of the smoke belt at latitudes 27°–31°N and 67°–71°N. For the OSU GCM we have mimicked this within the latitudes 28°–32°N and 68°–72°N.

The NCAR CCM is a nine-level general circulation model, and Covey *et al.* [1984, 1985] placed equal smoke optical depths within four of the model's layers, which approximately corresponds to employing a constant smoke mixing ratio for the altitude range from 1 to 10 km. Within the OSU GCM we have correspondingly placed equal smoke optical depths within all of the model's four radiation layers, which coincides to a constant smoke mixing ratio located between the surface and an altitude of approximately 11 km.

Since the NCAR CCM does not have a diurnal cycle, whereas the OSU GCM does, we have, solely for the purpose of this intercomparison, replaced the diurnal cycle within the OSU GCM with a latitudinally dependent fixed sun by using the same prescription as in the NCAR CCM.

The change in ground temperature, averaged over land areas for comparable latitude ranges, is shown in Figure 10 for the two models. Here we have much greater day 10 surface cooling than for the July $\tau = 3$ OSU GCM results which will next be shown in Figure 11. This is due to the different smoke single scattering albedos (0.7 for Figure 11 and 0 for Figure 10). As discussed by Cess [1985], to first order the direct surface forcing by smoke is dependent upon the absorption optical depth rather than the extinction (absorption plus scattering) optical depth. For optical depth 3 and a single scattering albedo of 0.7 the absorption optical depth is 0.9 (Figure 11), while for a single scattering albedo of zero, the optical depth 3 denotes the absorption optical depth (Figure 10), and this is the explanation for the differences between Figures 11 and 10.

Considering the very extreme manner in which the models have been forced, the degree of agreement between the NCAR CCM and the OSU GCM is not unreasonable. In view of the many differences in which physical processes are parameterized within the two models, it would be difficult to quantitatively explain the differences that do exist.

There is, however, one noteworthy difference. As Covey *et al.* [1985] point out, the parameterizations for energy transport by vertical diffusion within the CCM were derived for

near-neutral static stability, resulting in significant sensible heat transport to the surface whenever the surface potential temperature is lower than that of the overlying air, as is the case for the conditions of the present intercomparison. As a consequence of this, for day 10 of their simulation there is a 50 W m^{-2} net convective (latent plus sensible) heat flux to the surface (land average for 33°N to 60°N). (This subdivides into a sensible heat flux to the surface of 68 W m^{-2} and a latent heat flux from the surface of 18 W m^{-2} .)

The OSU GCM does incorporate, although admittedly in a crude fashion, a dependence of vertical diffusion upon atmospheric static stability, and for day 10 of the simulation the net convective heat flux to the land surface is only 6 W m^{-2} . In terms of a blackbody response the difference in this quantity between the two models, 44 W m^{-2} , would produce a ground temperature roughly 10°C warmer for the NCAR CCM as opposed to the OSU GCM. Although this could account for much of the difference shown in Figure 10, it would be premature, based upon only a single compared quantity, to conclude that the two general circulation models behave in a comparable manner.

We now turn to the intercomparison of the OSU GCM and the analog RCM, although it must first be emphasized that there are numerous problems associated with such a comparison. The most notable ones are summarized below.

1. The RCM essentially depicts a "land only" planet, whereas the oceans within the GCM supply heat to the atmosphere, and through advective processes, this heat results in a moderation of the land cooling [Covey *et al.*, 1984, 1985].

2. The RCM refers to an annual average, whereas the GCM simulations are for July. As previously pointed out, Covey *et al.* [1984, 1985] have indicated that a summer simulation produces the maximum climatic effect.

To partially compensate for the second factor, we have additionally performed GCM simulations for April (actually a perpetual April 1), since the 20° – 90°N averaged insolation at this time is nearly identical to the global average as employed within the RCM. Recall that this latitude range coincides with that over which the smoke optical depth is uniform within the GCM.

The day 10 responses of surface-air temperature for both the GCM (April and July) and RCM are illustrated in Figure 11. Note first that the GCM results for April are not substantially different than for July, but the divergence of the April and July curves with increasing τ suggest that a significant

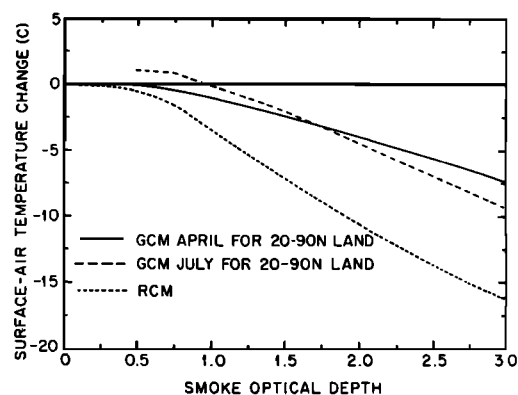


Fig. 11. Comparisons of the day 10 GCM and RCM changes in surface-air temperature as a function of smoke optical depth. The GCM results refer to 20° – 90°N averages over land and sea ice.

difference would exist for $\tau = 10$. Recall also that Covey *et al.* [1985] employed purely absorbing smoke having an absorption optical depth of 3; for our smoke single scattering albedo of 0.7 this is equivalent to a smoke extinction optical depth of 10. Thus in this context there is no apparent conflict between Figure 11 and the conclusion by Covey *et al.* that, for their single smoke loading, there is a strong seasonal dependence of the smoke-induced climate change. The results shown in Figure 11 would, however, suggest that their conclusion is restricted to large optical depths.

Figure 11 also illustrates a significant difference between the April GCM results and those of the RCM. Although much of this difference is attributable to the moderating effect of oceans within the GCM, there is another important difference. As we have repeatedly emphasized, the change in incident infrared radiation at the surface plays a key role in a climate model's response to smoke injection, and this will in turn be dependent upon the response of the model's vertical distribution of atmospheric water vapor. The GCM and RCM treat such changes in vastly different ways; within the RCM, atmospheric water vapor content is governed by the simplistic assumption of fixed relative humidity, whereas the GCM contains a hydrological cycle. Unfortunately, it is not possible to isolate this contribution to the differences shown in Figure 11, since the incident infrared surface radiation will also include, through ocean-land advective processes, effects resulting from ocean moderation of land cooling.

As a final point concerning model intercomparisons, we have employed within the RCM a constant vertical smoke density, a smoke optical depth of 3, a smoke single scattering albedo of 0.5, and a dust optical depth of 1, all of which are nearly consistent with Turco *et al.* [1983] for roughly the first 10 days of their baseline scenario. In that their model does not contain a boundary layer, in order to obtain further intermodel consistency, we have employed the version of our RCM that does not contain the boundary layer parameterization, as discussed in section 4. For day 10 we obtain a 31°C reduction in surface temperature, consistent with the day 10 result of Turco *et al.* (approximately 30°C from their Figure 2).

6. GENERAL CIRCULATION MODEL RESULTS

A more detailed description of the GCM results is now provided in terms of two sets of experiments. First, a discussion of the model's climate response to smoke injection is given that employs the same smoke model as used in the prior sections (0.55- μm single scattering albedo of 0.7 together with a constant vertical smoke mixing ratio), and second, a sensitivity study is presented in which these smoke parameters are varied. An important purpose of this analysis is to interpret the GCM results in terms of the feedback processes elucidated in the RCM study.

Model Behavior

As for the RCM, a progressive increase in smoke optical depth produces an associated decrease in surface latent plus sensible heat flux that is illustrated in Figure 12. In contrast to Figure 5, this flux is here defined as positive when heat is transferred upward from the surface. The corresponding changes in zonally averaged surface-air temperature are shown in Figure 13. With reference to both figures we may recall that the smoke optical depth increases with latitude from a value of zero near the equator to a constant value for 20°–90°N (see Table 1), and this accounts for the low-latitude variability of Figures 12 and 13.

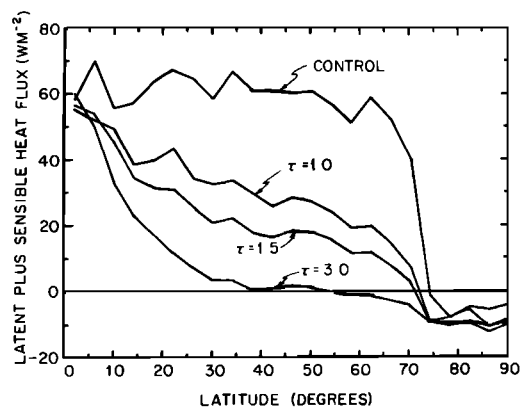


Fig. 12. Zonally averaged (over land and sea-ice areas) July surface latent plus sensible heat flux for the control climate and for various smoke optical depths. All results refer to day 10 following the smoke injection.

The mid-latitude variability exhibited in Figure 13 is influenced by the previously discussed initial condition dependence, as illustrated in Figure 1. For increasing optical depth, many of the mid-latitude features appearing in Figure 13 are preserved, and this appears to be due to preserved synoptic coherence over the short 10-day runs.

For the larger optical depths the sharp lessening in land and sea-ice cooling poleward of 55°N is a consequence of a slow transient response at high latitudes. To illustrate this, we have extended the $\tau = 3$ simulation to day 30, and the resulting time sequence of zonally averaged land and sea-ice temperatures shown in Figure 14 clearly illustrates the slow response at high latitudes. This is not a consequence of sea-ice formation, since sea ice extent and thickness are both fixed in this version of the GCM.

This lack of a significant day 0 to day 10 high-latitude response is due to the corresponding high snow/ice surface albedo. As discussed with reference to the RCM results of Figure 7, the very rapid initial response of the RCM is the result of the initial reduction in surface absorbed solar radiation, and this is consistent with the mid-latitude GCM response of Figure 14. But at high latitudes the large surface albedo significantly diminishes this initial direct surface forcing. In proceeding from day 10 to day 30 there is found to be a significant reduction in high-latitude incident infrared radiation at the surface, indicating that the corresponding tran-

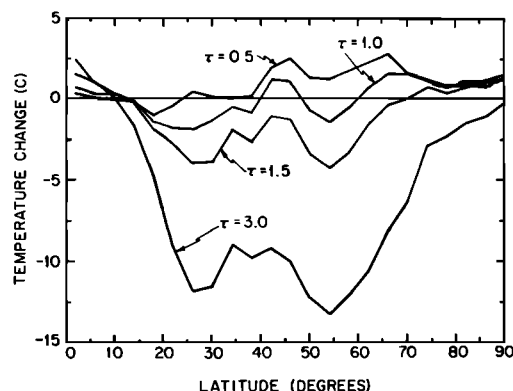


Fig. 13. Zonally averaged (over land and sea-ice areas) day 10 changes in July surface-air temperature for various smoke optical depths.

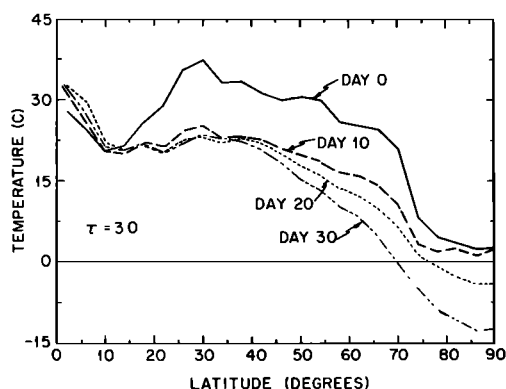


Fig. 14. Time history of zonally averaged (over land and sea-ice areas) July surface-air temperature for a smoke optical depth of 3. Day 0 refers to the control climate.

sient response shown in Figure 14 is associated with atmospheric processes.

Regional reductions of day 10 surface-air temperature are shown in Figure 15. As should be expected, maximum cooling occurs in interior continental regions.

But it must be emphasized that the results summarized in Figures 12–15 cannot be interpreted as predictive of events following a nuclear exchange. The present invariance of the smoke optical depth over time and longitude was chosen purely for illustrative purposes. Furthermore (and this is a point that must be addressed by those who attempt predictive studies), the quantitative nature of the results shown in Figures 12–15 will be dependent upon initial conditions, as has already been illustrated in Figure 1 with reference to zonal averages. The sole intent here has been to obtain a qualitative understanding as to how a GCM responds to a most unusual climate forcing mechanism.

Sensitivity Studies

Turning next to sensitivity studies, the change in surface-air temperature over land and sea ice areas is illustrated in Figure 16 for two different vertical smoke distributions: a constant smoke mixing ratio and a constant smoke density. As in prior studies [e.g., *Ramaswamy and Kiehl, 1985*], a more severe climatic impact occurs when the smoke is located higher in the

atmosphere (constant density as opposed to constant mixing ratio). This is partially due to solar absorption occurring higher in the atmosphere, so that there is reduced infrared radiation incident at the surface. But this in turn leads to a reduction in net surface absorption that further reduces sensible and latent heat fluxes at the surface and increases convective decoupling of the troposphere and surface, thus enhancing the transition from direct surface-troposphere forcing (heating) to direct surface forcing (cooling). In other words, through interactive feedback processes there is a change in the relative importance of the two competing forcing mechanisms associated with a change in smoke vertical distribution.

This explains why there is a proportionately greater impact of the smoke vertical distribution for $\tau = 1.5$ than for $\tau = 3.0$. In the latter case the moderating effect of surface-troposphere heating is insignificant, so that the changes shown in Figure 16 are due solely to the change in infrared radiation incident upon the surface. But for $\tau = 1.5$ this is augmented, in going from constant smoke mixing ratio to constant smoke density, by the associated reduction of direct surface-troposphere forcing relative to direct surface forcing. Further discussion of this point is given below with reference to Figure 18.

The effect of reducing the smoke single scattering albedo from 0.7 to 0.5 is illustrated in Figure 17. Here again we have interactive feedback mechanisms at work. For $\tau = 1$, very little happens when the single scattering albedo is changed. Since a reduction of single scattering albedo corresponds to an increase in absorption optical depth, this leads to an enhancement of both direct surface-troposphere heating and direct surface cooling. But for $\tau = 1$ these two competing forcing mechanisms are in near compensation, and this compensatory effect is only slightly impacted by the reduction of the single scattering albedo. For $\tau = 3$, on the other hand, it is direct surface cooling that is the dominant forcing mechanism, such that the climate response is now more sensitive to a change in single scattering albedo.

However, the compensation of direct forcing mechanisms for $\tau = 1$ is dependent upon the smoke's vertical distribution. Figure 18 illustrates, again for $\tau = 1$, that there is a strong dependence upon single scattering albedo for constant smoke density, in contrast to a constant smoke mixing ratio. With reference to the discussion of Figure 16, raising the smoke to higher altitudes enhances the transition from direct surface-troposphere forcing to direct surface forcing, with the latter therefore dominating the constant density results of Figure 18,

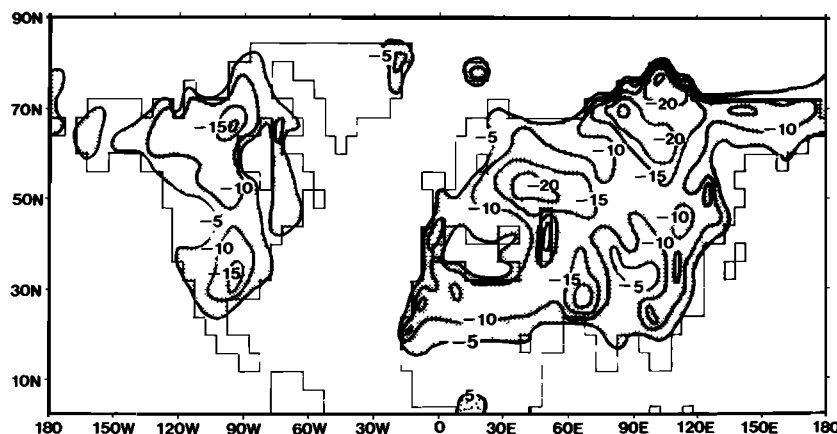


Fig. 15. Day 10 changes in July surface-air temperature caused by injected smoke with an optical depth of 3. Temperature contours are drawn for every 5°C, with the zero isotherm omitted.

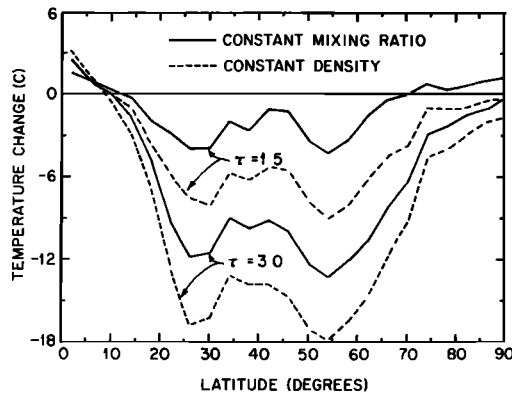


Fig. 16. Zonally averaged (over land and sea-ice areas) day 10 changes in July surface-air temperature for different vertical smoke distributions.

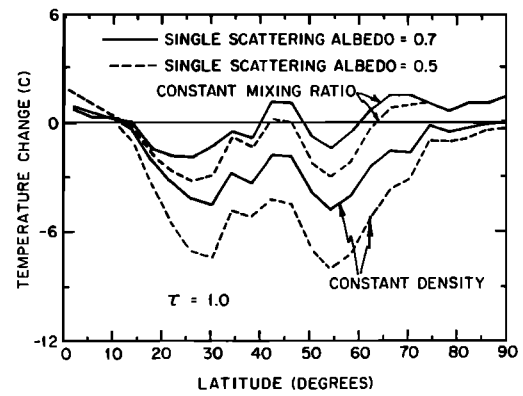


Fig. 18. Zonally averaged (over land and sea-ice areas) day 10 changes in July surface-air temperature for simultaneous changes of the vertical smoke distribution and the smoke single scattering albedo. The smoke optical depth is 1.0.

and this explains the stronger dependence upon single scattering albedo for this vertical distribution.

A further aspect of Figure 18 concerns the so-called “threshold problem,” for which it is commonly stated that $\tau = 1$ is the critical optical depth for the onset of significant cooling (see discussion by Cess [1985]). This is an important issue here for two reasons: first, with respect to the magnitude of a nuclear exchange that would produce significant climatic effects, and second, with regard to estimating the long-term climatic impact of a large exchange. From Figure 18 it is obvious that such a threshold is strongly dependent upon how “knobs are twisted” within a model.

As a final point, two simulations have been performed with the inclusion of stratospheric dust, the optical properties of which are described in the appendix. These results are shown in Figure 19 for a smoke optical depth of 3 and a dust optical depth of 1, the latter having the same latitudinal distribution as for smoke (see Table 1). As would be expected the presence of dust leads to further cooling as a consequence of its back-scattering of solar radiation.

7. CONCLUSIONS

It is again emphasized that the sole intent of this paper has been to investigate the qualitative nature and behavior of climate forcing mechanisms and climate feedback processes associated with the injection of atmospheric smoke and dust. In

this regard the analog RCM has proven to be a valuable tool in interpreting and understanding processes occurring within the GCM.

A primary conclusion is that the climate response to atmospheric smoke injection is far more complex than for the more familiar CO_2 -climate problem, which one may conceptually envision as a response to a single direct forcing (surface-troposphere heating), and for which feedback mechanisms are primarily associated with the response process.

Atmospheric smoke injection, on the other hand, produces two distinctly different climate forcing mechanisms that act in opposition to one another: direct surface-troposphere heating and direct surface cooling. Moreover, the transition from dominance by one to dominance by the other is governed through an interactive feedback process associated with the change in infrared radiation at the surface, a process that plays two roles in that it also significantly impacts the climate response to the dual and competing direct forcing mechanisms.

Convective mixing processes also play an important role, since the forcing mechanism transition is dependent upon convective decoupling of the surface and atmosphere as a result of the smoke-induced increase in atmospheric static stability. Thus both convective and surface radiative processes play key roles in a climate model's forcing/response behavior associated with convective surface-atmosphere decoupling caused by the

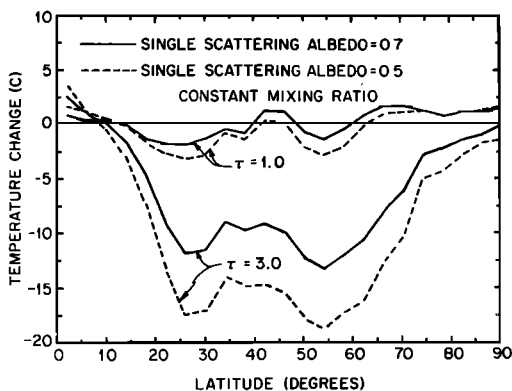


Fig. 17. Zonally averaged (over land and sea-ice areas) day 10 changes in July surface-air temperature for different smoke single scattering albedos.

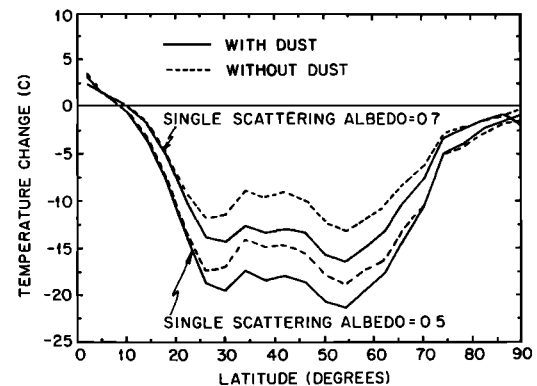


Fig. 19. Zonally averaged (over land and sea-ice areas) day 10 changes in July surface-air temperature showing the impact of stratospheric dust. The dust optical depth is 1.0, while for the smoke it is 3.0.

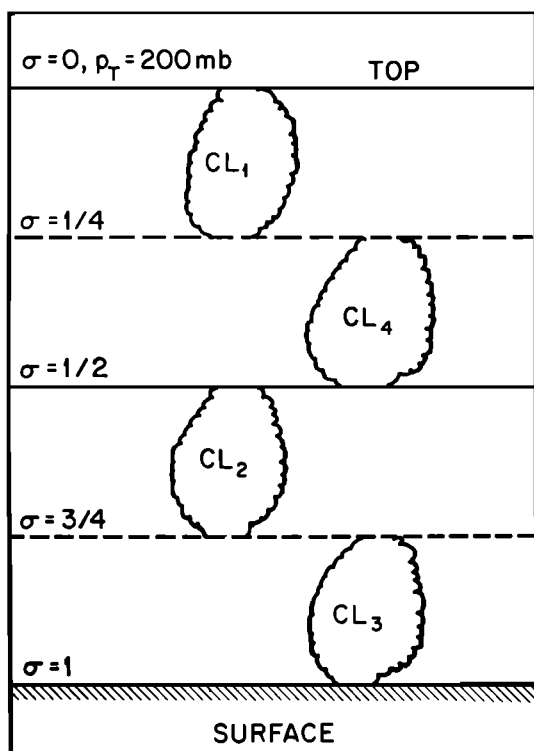


Fig. 20. A schematic illustration of the vertical structure of the OSU GCM. Cloud types CL_2 and CL_4 depict large-scale cloudiness, while CL_1 and CL_3 result from convective motion (see section 2).

injection of atmospheric smoke. It is again emphasized that there is no parallel to this in the more conventional CO_2 -climate problem, for which such convective decoupling is not an issue.

In view of the above we endorse the recommendations of Covey *et al.* [1985] as to the need to improve, within general circulation models, parameterizations of the planetary boundary layer, surface processes, and subgrid-scale vertical convection. We add to this list infrared radiative transfer algorithms, since most general circulation models treat surface infrared radiation in a relatively simplistic fashion, whereas, as we have repeatedly emphasized, this process plays a key role with respect to climatic change induced by atmospheric smoke.

APPENDIX

As discussed in the text the solar radiation routine within the OSU GCM [Ghan *et al.*, 1982] was replaced by a delta-Eddington model in order to accommodate the inclusion of large quantities of atmospheric smoke and dust. In essence this solar radiation model closely follows that described by Cess [1985], but with the following modifications.

1. Solar absorption by atmospheric water vapor has been explicitly incorporated by using the exponential sum-fit method.
2. The model has been extended to include scattering and absorption of solar radiation by clouds.
3. Computational efficiency has been enhanced through the determination of two representative wavelengths at which the solar transmittance and absorptance calculations are performed.

The location of clouds in the present version of the OSU

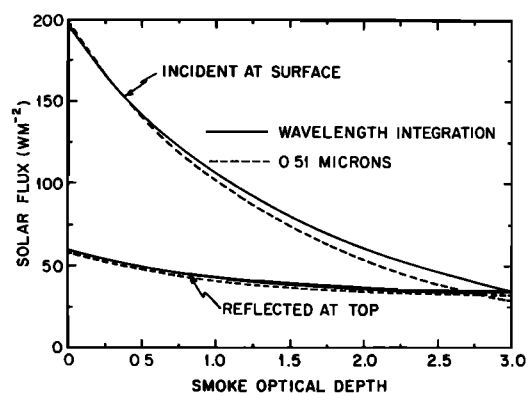


Fig. 21. Comparison of $\lambda < 0.9 \mu m$ solar flux calculations performed using a wavelength integration and a monochromatic ($0.51 \mu m$) atmospheric transmittance and absorptance evaluation.

GCM is illustrated in Figure 20 (see also section 2). Although the primary prognostic variables are calculated at only two levels ($\sigma = 1/4, 3/4$), through interpolation [Ghan *et al.*, 1982] clouds are formed in half layers of $1/4 \sigma$ depth, and the radiation computations, in turn, are performed for the corresponding four layers. The cloud types illustrated in Figure 20 coincide with those in the original version of the model [Schlesinger and Gates, 1980], except that cloud-type CL_3 is here assumed to completely fill the lowest half layer, in contrast to the original version for which CL_3 comprised a thin cloud at $\sigma = 3/4$. This modification was necessary to be consistent with the delta-Eddington method.

The model does not consider fractional cloudiness, meaning that any of the four cloud types are either totally present or totally absent at a given model grid point. There are also constraints as to the coexistence of cloud types [Ghan *et al.*, 1982]. Moreover, cloud types CL_2 , CL_3 , and CL_4 are designated as As, Cu, and As (i.e., water clouds), respectively, if the average layer temperature exceeds $-40^\circ C$, whereas when the layer temperature is below this value the clouds are designated as Ci (i.e., ice clouds).

The smoke-dust solar radiation model of Cess [1985] was employed to select two representative wavelengths at which atmospheric transmittance and absorptance calculations are performed. As in the original solar radiation calculation, the

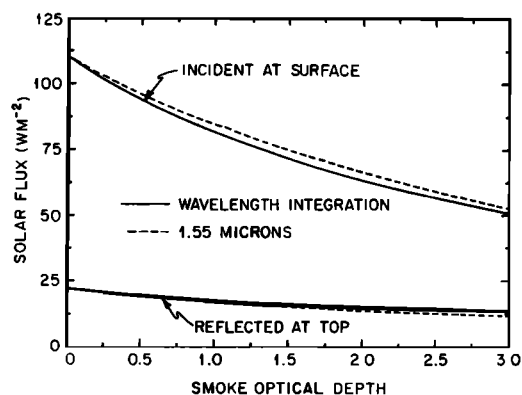


Fig. 22. Comparison of $\lambda > 0.9 \mu m$ solar flux calculations performed using a wavelength integration and a monochromatic ($1.55 \mu m$) atmospheric transmittance and absorptance evaluation.

TABLE 2. Optical Properties of Atmospheric Smoke and Dust, Where g Denotes the Asymmetry Factor and ω is the Single Scattering Albedo

Quantity	$\lambda = 0.51 \mu\text{m}$		$\lambda = 1.55 \mu\text{m}$	
	g	ω	g	ω
Smoke I	0.706	0.705	0.659	0.552
Smoke II	0.706	0.504	0.659	0.394
Dust	0.632	1.000	0.573	1.000

solar spectrum is split into two wavelength regions at $0.9 \mu\text{m}$. Representative wavelengths for each region are then determined so that the solar fluxes at both the top of the atmosphere and at the surface are in near agreement with the wavelength integrated values. For $\lambda < 0.9 \mu\text{m}$ the interactive effects of Rayleigh scattering, smoke and dust are essentially reproduced by evaluating the atmospheric transmittance and absorptance at the single wavelength of $0.51 \mu\text{m}$, while for $\lambda > 0.9 \mu\text{m}$ the effective wavelength is $1.55 \mu\text{m}$. Figures 21 and 22 illustrate, for $\lambda < 0.9 \mu\text{m}$ and $\lambda > 0.9 \mu\text{m}$, respectively, the agreement between the single-wavelength calculations and the wavelength-integrated fluxes for the case of smoke addition to the atmosphere. These comparisons refer to the variation with smoke optical depth of reflected solar radiation at the top of the model atmosphere and that incident at the surface. These fluxes are global averages, including Rayleigh scattering, and the surface albedo is 0.2. Similar agreement exists for the incorporation of atmospheric dust, corresponding to case I of Cess [1985].

The optical properties of smoke and dust, as employed in the present study, are summarized in Table 2 for the two representative wavelengths of $0.51 \mu\text{m}$ and $1.55 \mu\text{m}$, where g denotes the asymmetry factor and ω is the single scattering albedo. Smoke I is the same smoke model employed by Cess [1985], and this has a single scattering albedo of 0.7 at $0.55 \mu\text{m}$, a value close to the *National Academy of Sciences* [1984] smoke model. For Smoke II this number is reduced to 0.5, which more closely coincides with that employed by Turco *et al.* [1983].

Dust is placed solely in the stratosphere. Since the GCM does not have an explicit stratosphere, it is necessary to assume that the dust is nonabsorbing, i.e., it has a single scattering albedo of unity. But suggested values are close to this (e.g., the *National Academy of Sciences* [1984] value is 0.98). The asymmetry factors for dust, listed in Table 2, are from Cess [1985].

Two vertical smoke distributions are employed within the

TABLE 3. Vertical Distributions of the Ratio of τ/τ_{vis} for Smoke, Where τ_{vis} Denotes the Value of τ at $0.55 \mu\text{m}$

Layer	Constant Smoke Mixing Ratio		Constant Smoke Density	
	$\lambda = 0.51 \mu\text{m}$	$\lambda = 1.55 \mu\text{m}$	$\lambda = 0.51 \mu\text{m}$	$\lambda = 1.55 \mu\text{m}$
$\sigma = 0-1/4$	0.270	0.071	0.465	0.122
$\sigma = 1/4-1/2$	0.270	0.071	0.272	0.072
$\sigma = 1/2-3/4$	0.270	0.071	0.193	0.051
$\sigma = 3/4-1$	0.270	0.071	0.150	0.039
Total	1.080	0.284	1.080	0.284

TABLE 4. Cloud Optical Properties for Wavelengths Less Than $0.9 \mu\text{m}$

Cloud Type	τ	g	ω
CL ₁	12	0.84	1.0
CL ₂ , As	7	0.84	1.0
CL ₂ , Ci	2	0.84	1.0
CL ₃ , Cu	12	0.84	1.0
CL ₃ , Ci	2	0.84	1.0
CL ₄ , As	7	0.84	1.0
CL ₄ , Ci	2	0.84	1.0

model; a constant smoke mixing ratio and a constant smoke density. The smoke optical depths, referenced to that at $0.55 \mu\text{m}$, are listed in Table 3 for each of the model's four radiation layers.

With respect to the incorporation of clouds, the cloud optical properties were, in part, determined by matching the globally averaged cloud reflectances and absorptances produced by the delta-Eddington method to the zenith-angle-independent reflectances and absorptances utilized in the original OSU GCM solar radiation routine. For $\lambda < 0.9 \mu\text{m}$ the clouds are nonabsorbing, and the asymmetry factor is taken to be 0.84 [Hansen, 1969]. The cloud optical depths were then determined by matching cloud reflectances; this information is summarized in Table 4. The same optical depths were utilized for $\lambda > 0.9 \mu\text{m}$, whereas the asymmetry factors and single scattering albedos were evaluated by matching both cloud reflectances and absorptances. These are summarized in Table 5.

To incorporate solar absorption by atmospheric water vapor, a six-term exponential sum fit for solar absorption by atmospheric water vapor, as presented by Somerville *et al.* [1974], was utilized. This expresses the water vapor solar transmittance T for a given level as

$$T = \sum_{m=1}^6 p_m e^{-k_m y} \quad (\text{A1})$$

where y is the scaled water vapor amount for that level, evaluated as in the original OSU GCM solar radiation routine [Ghan *et al.*, 1982]. The coefficients p_m and k_m are summarized in Table 6. The use of the exponential sum fit is necessary for consistency with the delta-Eddington method. Wavelengths less than $0.9 \mu\text{m}$ are denoted by $m = 1$, with $p_1 = 0.647$ representing the fraction of solar radiation at wavelengths less than $0.9 \mu\text{m}$.

The evaluation of the reflectance and transmittance of each of the five atmospheric layers (four model layers plus stratospheric dust) follows the procedure outlined in the appendix of Cess [1985], as does the subsequent combination of layers.

TABLE 5. Cloud Optical Properties for Wavelengths Greater Than $0.9 \mu\text{m}$

Cloud Type	τ	g	ω
CL ₁	12	0.60	0.982
CL ₂ , As	7	0.76	0.983
CL ₂ , Ci	2	0.82	0.990
CL ₃ , Cu	12	0.60	0.982
CL ₃ , Ci	2	0.82	0.990
CL ₄ , As	7	0.76	0.983
CL ₄ , Ci	2	0.82	0.990

TABLE 6. Exponential Sum Fit Coefficients for Water Vapor Absorption [Somerville et al., 1974]

m	k_m	p_m
1	0.00007	0.647
2	0.005	0.107
3	0.041	0.104
4	0.416	0.073
5	4.75	0.044
6	72.5	0.025

Acknowledgments. We thank M. E. Schlesinger of Oregon State University for providing us with an earlier version of the RCM, M. C. MacCracken for suggesting improvements in the manuscript, and A. R. Licuanan for programming assistance. Support for this work was provided by the U.S. Department of Energy through contract W-7405-ENG-48 to Lawrence Livermore National Laboratory and by the National Science Foundation through grant ATM8212791 to SUNY Stony Brook and grant ATM8205992 to Oregon State University.

REFERENCES

- Aleksandrov, V. V., and G. L. Stenchikov, On the modelling of the climatic consequences of the nuclear war, in *The Proceedings on Applied Mathematics*, 21 pp., The Computing Centre of the USSR Academy of Sciences, Moscow, 1983.
- Cess, R. D., Climatic change: An appraisal of atmospheric feedback mechanisms employing zonal climatology, *J. Atmos. Sci.*, **33**, 1831–1843, 1976.
- Cess, R. D., Nuclear war: Illustrative effects of atmospheric smoke and dust upon solar radiation, *Clim. Change*, **7**, 237–251, 1985.
- Coakley, J. A., Jr., R. D. Cess, and F. B. Yurevich, The effect of tropospheric aerosols on the earth's budget: A parameterization for climate models, *J. Atmos. Sci.*, **40**, 116–138, 1983.
- Covey, C., S. H. Schneider, and S. L. Thompson, Global atmospheric effects of massive smoke injections from a nuclear war: Results from general circulation model simulations, *Nature*, **308**, 21–25, 1984.
- Covey, C., S. L. Thompson, and S. H. Schneider, "Nuclear winter": A diagnosis of atmospheric general circulation model simulations, *J. Geophys. Res.*, **90**(D3), 5615–5628, 1985.
- Crutzen, P. J., and J. W. Birks, The atmosphere after a nuclear war: Twilight at noon, *Ambio*, **11**, 114–125, 1982.
- Crutzen, P. J., I. E. Galbally, and C. Brühl, Atmospheric effects from post-nuclear fires, *Clim. Change*, **6**, 323–364, 1984.
- Dickinson, R. E., Modeling climate changes due to carbon dioxide increases, in *Carbon Dioxide Review*, edited by W. C. Clark, pp. 101–133, Clarendon, New York, 1982.
- Ghan, S. J., J. W. Lingaas, M. E. Schlesinger, R. L. Mobley, and W. L. Gates, A documentation of the OSU two-level atmospheric general circulation model, *Rep. 61*, 391 pp., Clim. Res. Inst., Oregon State Univ. Corvallis, Oreg., 1982.
- Hansen, J. E., Exact and approximate solutions for multiple scattering by cloudy and hazy planetary atmospheres, *J. Atmos. Sci.*, **26**, 478–487, 1969.
- MacCracken, M. C., Nuclear war: Preliminary estimates of the climatic effects of a nuclear exchange, *Rep. UCRL-89770*, 23 pp., Lawrence Livermore Nat. Lab., Livermore, Calif., 1983.
- MacCracken, M. C., and J. J. Walton, The effects of interactive transport and scavenging of smoke on the calculated temperature change resulting from large amounts of smoke, *Rep. UCRL-91446*, 20 pp., Lawrence Livermore Nat. Lab., Livermore, Calif., 1984.
- Manabe, S., and R. T. Wetherald, Thermal equilibrium of the atmosphere with a given distribution of relative humidity, *J. Atmos. Sci.*, **24**, 241–259, 1967.
- National Academy of Sciences, Environmental Effects of Nuclear Weapons, Report, Comm. on Atmos. Effects of Nucl. Explos., Washington, D. C., 1984.
- Potter, G. L., and R. D. Cess, Background tropospheric aerosols: Incorporation within a statistical-dynamical climate model, *J. Geophys. Res.*, **89**, 9521–9526, 1984.
- Ramaswamy, V., and J. T. Kiehl, Sensitivities of the radiative forcing due to large loadings of smoke and dust aerosol, *J. Geophys. Res.*, **90**(D3), 5597–5614, 1985.
- Robock, A., Snow and ice feedbacks prolong effects of nuclear winter, *Nature*, **310**, 667–670, 1984.
- Schlesinger, M. E., and W. L. Gates, The January and July performance of the OSU two-level atmospheric general circulation model, *J. Atmos. Sci.*, **37**, 1914–1943, 1980.
- Somerville, R. C., J., P. H. Stone, M. Halem, J. E. Hansen, J. S. Hogan, L. M. Druyan, G. Russell, A. A. Lacis, W. J. Quirk and J. Tenenbaum, The GISS model of the global atmosphere, *J. Atmos. Sci.*, **31**, 84–117, 1974.
- Thompson, S. L., V. V. Aleksandrov, G. L. Stenchikov, S. H. Schneider, C. Covey, and R. M. Chervin, Global climatic consequences of nuclear war: Simulations with three-dimensional models, *Ambio*, **13**, 236–243, 1984.
- Turco, R. P., O. B. Toon, T. Ackerman, J. B. Pollack, and C. Sagan, Nuclear winter: Global consequences of multiple nuclear explosions, *Science*, **222**, 1283–1292, 1983.
- R. D. Cess, Laboratory for Planetary Atmospheres Research, State University of New York, Stony Brook, NY 11794.
- W. L. Gates, Department of Atmospheric Sciences, Oregon State University, Corvallis, OR 97331.
- S. J. Ghan and G. L. Potter, Lawrence Livermore National Laboratory, University of California, Livermore, CA 94550.

(Received April 18, 1985;
revised September 10, 1985;
accepted September 10, 1985.)